ADVANCED FUNCTIONAL MATERIALS

Full Paper

Systematic Study of Oxygen Vacancy Tunable Transport Properties of Few-Layer MoO$_{3-x}$ Enabled by Vapor-Based Synthesis

By *Eve D. Hanson, Luc Lajaunie, Shiqiang Hao, Benjamin D. Myers, Fengyuan Shi, Akshay A. Murthy, Chris Wolverton, Raul Arenal, and Vinayak P. Dravid**

Bulk and nanoscale molybdenum trioxide (MoO$_3$) has shown impressive technologically relevant properties, but deeper investigation into 2D MoO$_3$ has been stymied by the lack of reliable vapor-based synthesis and doping techniques. Herein, the successful synthesis of high-quality, few-layer MoO$_3$ down to bilayer thickness via physical vapor deposition is reported. The electronic structure of MoO$_3$ can be strongly modified by introducing oxygen substoichiometry (MoO$_{3-x}$), which introduces gap states and increases conductivity. A dose-controlled electron irradiation technique to introduce oxygen vacancies into the few-layer MoO$_3$ structure is presented, thereby adding n-type doping. By combining in situ transport with core-loss and monochromated low-loss scanning transmission electron microscopy–electron energy-loss spectroscopy studies, a detailed structure–property relationship is developed between Mo-oxidation state and resistance. Transport properties are reported for MoO$_{3-x}$ down to three layers thick, the most 2D-like MoO$_{3-x}$ transport hitherto reported. Combining these results with density functional theory calculations, a radiolysis-based mechanism for the irradiation-induced oxygen vacancy introduction is developed, including insights into favorable configurations of oxygen defects. These systematic studies represent an important step forward in bringing few-layer MoO$_3$ and MoO$_{3-x}$ into the 2D family, as well as highlight the promise of MoO$_{3-x}$ as a functional, tunable electronic material.

1. Introduction

Molybdenum trioxide (MoO$_3$), a layered transition metal oxide, has shown widespread and increasing technological applicability due to its numerous attractive functional properties. Molybdenum oxides together represent an attractive class of oxides with a variety of valence states, crystal structures, and amorphous states.[1,2] MoO$_2$ typically has a monoclinic structure, while MoO$_3$ has three polymorphs: an orthorhombic phase (α-MoO$_3$, thermodynamically stable), a hexagonal phase (h-MoO$_3$), and a monoclinic phase (β-MoO$_3$). Among these phases, only α-MoO$_3$ has a stable layered structure; this paper exclusively focuses on this layered α-MoO$_3$ phase.

Bulk MoO$_3$ in stoichiometric form is a high-k dielectric ($k > 500$) insulator.[3] Further, the electronic structure of MoO$_3$ can be tailored by modifying the oxygen substoichiometry (MoO$_{3-x}$). Oxygen substoichiometry introduces electronic gap states and increased electrical conductivity.[4,5] These bulk tunable transport properties have shown applicability across a number of technological regimes, including as a promising electrochromic, battery cathode material, and gas sensor.[6] Recent excitement has been driven by the high work function (6.6 eV) and hole transport properties of MoO$_{3-x}$, which have been used to meaningfully improve conversion efficiencies for solar cells and OLEDs.[7]

Despite these numerous exciting bulk properties, MoO$_3$ has received limited attention in 2D form. Initial studies of 2D MoO$_3$ and MoO$_{3-x}$ have indicated great potential; few-layer MoO$_{3-x}$ has shown ultrahigh mobility (>1100 cm2

E. D. Hanson, Dr. S. Hao, B. D. Myers, Dr. F. Shi, A. A. Murthy, Prof. C. Wolverton, Prof. V. P. Dravid, Department of Materials Science and Engineering, Northwestern University, Evanston, IL 60208, USA
Dr. L. Lajaunie, Dr. R. Arenal, Laboratorio de Microscopias Avanzadas (LMA), Instituto de Nanociencia de Aragon, Universidad de Zaragoza , 50018 Zaragoza, Spain
B. D. Myers, Dr. F. Shi, Prof. V. P. Dravid, Northwestern University Atomic and Nanoscale Characterization Experimental (NUANCE) Center, Northwestern University, Evanston, IL 60208, USA
Dr. R. Arenal, ARAID Foundation , 50018 Zaragoza, Spain
Prof. V. P. Dravid, International Institute for Nanotechnology, Northwestern University, Evanston, IL 60208, USA
Q1
Correspondence to: Prof. V. P. Dravid (E-mail: v-dravid@northwestern.edu)
10.1002/adfm.201605380

Full Paper

Author Proof

V−1 s−1) due to high dielectric constant Coulomb scattering suppression.[8] Nanoscale MoO_{3-x} has also shown broadband photodetector response with high photoresponsivity.[9] Further, chemically exfoliated 2D MoO_{3-x} flakes have been shown to have high enough conductivities to sustain plasmonic resonances in the visible regime and can be made into conductive inks.[10,11] MoO_3 has also been used to modify other 2D materials in advantageous ways. Thin films of MoO_3 have been used to hole dope graphene and improve contact resistance for MoS_2.[12,13] These preliminary findings indicate that 2D MoO_3 would be a beneficial material to incorporate within interacting, multicomponent 2D heterostructures.

However, progress in 2D MoO_3 devices has been stalled in part due to the lack of large-area, "electronic-grade" syntheses. Initial structural and electronic studies have been conducted on sheets fabricated via mechanical exfoliation, chemical exfoliation, or hydrothermal means, but these techniques suffer from low yield, high defect densities, and organic contaminants, respectively.[10,14,15] Physical vapor deposition directly on SiO_2 substrates allows for rapid identification of few-layer samples as well as provide high-quality samples ready for broader characterization and device integration.[16]

In this work, we report a physical vapor deposition synthesis of few-layer MoO_3 directly onto SiO_2 substrates. These few-layer nanosheets are of high quality, as confirmed by a number of techniques including high-resolution transmission electron microscopy (HRTEM, gives structural information), scanning electron microscopy (SEM, gives morphology information), atomic force microscopy (AFM, gives higher resolution morphology information), and Raman spectroscopy (gives characteristic phonon mode information). We also explore the electronic structure changes due to 2D confinement. Density functional theory (DFT) calculations show that monolayer confinement of MoO_3 leads to a modest increase in the bandgap.

The critical substoichiometry that underlies MoO_{3-x}-based technologies has typically been induced by a H^+ ion posttreatment.[4,8] However, these H^+ ion-based processes are difficult to control and quantify. A more quantifiable oxygen vacancy introduction process could provide a more coherent link between the MoO_{3-x} structure and transport properties. We report a dose-controlled electron-beam irradiation technique to introduce vacancies into few-layer MoO_3.

Prior transmission electron microscopy (TEM) studies have indicated that bulk or nanostructured MoO_3 can be reduced to MoO_{3-x} and MoO_2 via electron-beam irradiation.[17,18] In recent years, electron irradiation has offered the possibility of engineering materials at the nanoscale.[19,20] Building on these preliminary studies and invoking in situ transport studies, we provide a detailed structure–transport correlation between electron-beam irradiation-induced oxygen vacancy introduction and resultant n-type doping across a variety of MoO_{3-x} layer numbers, down to trilayer thickness. In situ core-loss and monochromated low-loss electron energy-loss spectroscopy (EELS) studies provide quantitative insights into the chemistry and bandgap changes during the evolution of the few-layer MoO_3 into few-layer MoO_{3-x}, giving additional evidence of oxygen vacancy introduction during irradiation. Bringing these different characterization results and DFT calculations together, the Knotek–Feibelman mechanism of radi-
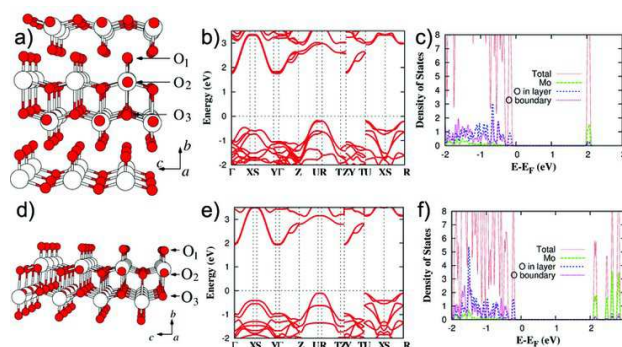

Figure 1. DFT calculated electronic structure of the bulk and monolayer MoO_3. a) Bulk structure with oxygen positions labeled, b) bulk electronic structure, and c) bulk density of states. d) Monolayer structure with oxygen positions labeled, e) monolayer electronic structure, and f) monolayer density of states. **Q2**

olysis is presented as the mechanism of oxygen vacancy and n-type carrier introduction. DFT calculations indicate which crystallographically distinct oxygen vacancies are most energetically favorable to form during the doping process.

Transport studies show the resistance of the MoO_{3-x} 2D sheet can be modified by over four orders of magnitude via controlled electron-beam doses. As such, MoO_{3-x} shows the properties of a highly tunable 2D functional material. The present work highlights the exciting potential of MoO_{3-x} as a functional component in fully 2D heterostructures as well as provides a synthesis technique to reliably fabricate MoO_3 and MoO_{3-x} in few-layer form.

2. Comparison of 2D and Bulk MoO_3 Electronic Structure

MoO_3 is an orthorhombic layered structure (space group *Pnma*), as indicated by **Figure 1**a. Each fundamental bilayer is comprised of two layers of distorted MoO_6 octahedra and is ≈1.4 nm thick. As shown in Figure 1a,d, there are three symmetrically inequivalent oxygen sites (red spheres) in α-MoO_3: a singly coordinated oxygen O_1, a doubly coordinated oxygen O_2, and a triply coordinated oxygen O_3. Each distorted Mo octahedra is comprised of an Mo atom (white sphere) bound to one O_1 atom, two O_2 atoms, and three O_3 atoms.

In stoichiometric form, MoO_3 has been experimentally determined to have a large indirect bandgap (≈3.2 eV).[2,21] DFT + U calculations were performed to give insight into the electronic structure of the monolayer form (Figure 1e) compared to the bulk form (Figure 1b). The bulk case shows an indirect bandgap of 1.96 eV, similar to other DFT + U studies of MoO_3.[22,23] The DFT-calculated electronic structure of an MoO_3 monolayer shows a slightly larger indirect bandgap of 2.03 eV. Quantum confinement effects in 2D materials often induce a more significant bandgap increase than we found in MoO_3.[24] To understand this relatively modest increase in bandgap, we examine the DFT-calculated density of states for

both the bulk and monolayer, as shown in Figure 1c,f. Since the valence band minimum (VBM) and conduction band maximum (CBM) states are dominated by states from the Mo and position O_2 and O_3 oxygen atoms, which are screened from confinement effects, monolayer confinement only leads to small changes in the electronic structure. The terminal oxygen atoms (O_1 position in Figure 1a) would experience the strongest confinement effects, but only have a minor contribution to the CBM and VBM. This simple structural argument explains why the bandgap of MoO_3 is only modestly affected by 2D nanostructuring.

3. Vapor-Based Synthesis of Few-Layer MoO_3

Few-layer MoO_3 sheets were grown via low-pressure physical vapor deposition (PVD). The deposition experimental setup is shown in Figure S1 (Supporting Information). MoO_3 powder is placed in the hot zone of the furnace and carried downstream with a dry air carrier gas. Dry air carrier gas is crucial to maintain oxygen stoichiometry and deposit the layered MoO_3 structure (vs. using an inert carrier gas to deposit monoclinic MoO_2). The growth is carried out at 700 C for <5 min and then quickly quenched by opening the furnace to stop further growth. The synthesis method produces a range of thicknesses of MoO_3 sheets. By using 300 nm SiO_2/Si substrates, few-layer samples are easily identified by optical contrast, similar to other 2D materials.[16]

Figure 2 shows structural characterization of the resultant bi- and few-layer MoO_3 samples. Figure 2a displays an optical micrograph corresponding to the AFM and SEM images in Figure 2b,c. The synthesized nanosheets are continuous and of high quality, with domain sizes on the order of 10 μm. The thickness has been determined by AFM analysis to be 3 nm, which corresponds to a bilayer. Figure 2d shows a TEM image of another few-layer sheet. The indexing of the selected area diffraction pattern (inset of Figure 2d) confirms the orthorhombic structure in the *Pnma* symmetry. An HRTEM image of the MoO_3 lattice fringes is shown in Figure 2e. While there is indication of beam damage, which will be explored in more detail below, the HRTEM micrograph confirms the good crystal quality of these flakes.

Raman spectroscopy was used to probe the changes in phonon modes as a result of extreme geometric confinement and high surface to volume ratios in the 2D crystals. Figure S2 (Supporting Information) shows the Raman spectra of the grown MoO_3 sheets of various thicknesses. As the thickness of the sheets decreases, the overall intensity of the Raman scattering decreases in lockstep. The ultrathin 4 nm sheets still show the key MoO_3 Raman modes, which serve as an additional confirmation of the MoO_3 structure. There is some disagreement in the literature about how to index the MoO_3 peaks and their physical interpretation.[25, 26] The Raman modes here were indexed based on the assignments reported by Camacho-López et al.[26] Beyond the traditionally indexed MoO_3 vibrational modes, an additional peak at ≈618 cm^{-1} was observed. This peak has been attributed to the hydrated form of MoO_3,
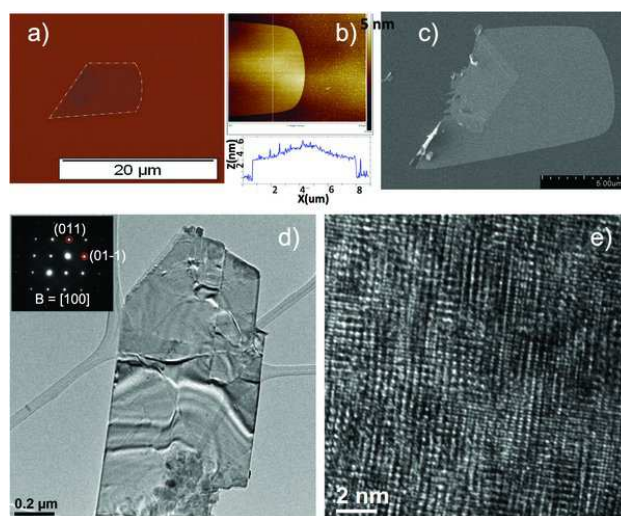

Figure 2. Structural characterization of 2D MoO_3. a) Optical image of a bilayer MoO_3, b) corresponding AFM image showing 3 nm height corresponding to bilayer thickness, and c) corresponding SEM image. d) TEM image of few-layer sample, inset shows diffraction pattern indexed to *Pnma* crystal structure. e) HRTEM image showing MoO_3 lattice fringes and beam damage.

which suggests there may be some surface hydration experienced by the few-layer sheets.[14]

4. Electron Irradiation-Induced Formation of Few-Layer MoO_{3-x}

In the 2D form, substoichiometry has been introduced to date via H$^+$ ions.[8] Due to the environmental sensitivity of 2D MoO_3, device fabrication is difficult. As a result, transport properties of MoO_3 have only been reported in the published literature for thicknesses greater than 6 nm.[8, 27] An in situ low dose electron-beam irradiation technique was developed to introduce oxygen vacancies controllably and quantifiably and to overcome these fabrication difficulties.

4.1. In Situ Transport Studies

In order to investigate the tunable transport properties of the PVD-grown 2D MoO_3, in situ transport measurements were performed with a nanoprobe station inside an SEM. This station allows us to bring conductive probes directly in contact with the sample and measure resistance as a function of electron dose. This gives us the ability to forego the frequently damaging lithographic device fabrication process and to probe the pristine intrinsic properties of the MoO_3 nanosheets.

Figure 3a shows these in situ nanoprobes in contact with an MoO_3 nanosheet. Figure 3b shows example current–voltage (*I*–*V*) curves for a 5 nm thick sheet as a function of different electron doses. The electron dose is introduced via carefully timed exposures and the electron-beam is blanked during electrical transport measurements. Before exposure, the current is
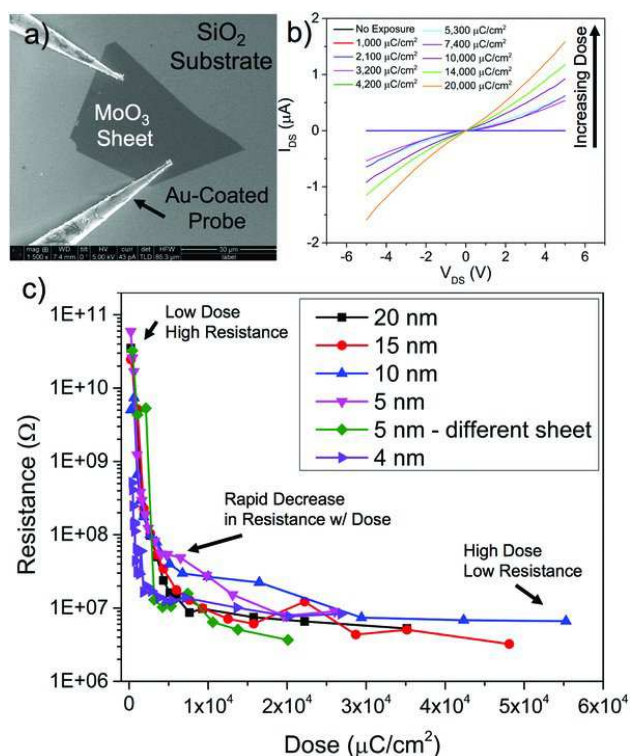
Author Proof

Full Paper

Figure 3. Electrical characterization of few-layer MoO_3 as a function of electron dose. a) SEM image of nanoprobes in contact with 20 nm MoO_3 sheet. b) Current–voltage (*I–V*) curves at a number of doses for a 5 nm MoO_3 sheet. c) Resistance as a function of electron dose across a number of MoO_3 thicknesses.

in the subnanoamp regime (a 5 nm thick example is shown in Figure S3a, Supporting Information). The *I–V* curves show a dramatic increase in current as a function of electron-beam dose. In the 5 nm case, after an electron dose > 3000 $\mu C\,cm^{-2}$, there is a jump in current of over three orders of magnitude compared to before irradiation. This rise in current continues with dose before gradually saturating. After irradiation, the *I–V* curves are generally linear and ohmic in character. In order to rule out carbon contamination as the new transport route, we measured *I–V* curves immediately adjacent to an exposed flake in the area of exposure. This adjacent area of SiO_2 with carbon contamination showed sub-nanoamp current even after an electron dose $>75\,000$ $\mu C/cm^2$ (shown in Figure S4). Given such low current, the influence of carbon contamination on 2D MoO_{3-x} transport properties can thus be excluded.

The resistance as a function of electron-beam dose has been measured across a number of flake thicknesses, as shown in Figure 3c. Resistance is reported for flakes down to trilayer (4 nm) thickness. Across the flake thicknesses, there is an exponential decay in resistance as a function of dose, and then at higher doses, saturation is present. There is no clear thickness dependence in the final resistance value.

In the semi-classical Boltzmann transport model, for a given order of magnitude drop in resistance we expect a similar magnitude increase in carrier concentration. Carrier concentration

effects on resistance were calculated from the Boltzmann transport equation, as shown in Figure S5b (Supporting Information). To put the comparison in similar terms, both the experimental and theoretical changes are calculated in terms of relative resistance. The relative resistances in Figure S5a (Supporting Information) were indexed to the most resistive sheet (5 nm, no electron dose). Figure S5b (Supporting Information) was indexed to 10^{15} carriers cm^{-3}, which has previously been reported to be the carrier concentration of stoichiometric MoO_3.[28] As expected, higher carrier concentrations correlate to lower relative resistances. Comparing the resistance changes in the experimental and theoretical data, we extrapolate that after the MoO_3 nanosheets are irradiated with doses greater than $10\,000$ $\mu C\,cm^{-2}$, the carrier concentration has increased to over 10^{18} carriers cm^{-3}. This result highlights the tunable nature of the irradiated 2D MoO_3 nanosheets.

Raman spectroscopic studies as a function of dose were also investigated (as shown in Figure S5c,d, Supporting Information). A number of 10 nm thick nanosheets were exposed to a variety of doses across the dose range shown in Figure S5c (Supporting Information). The electron dose exposure suppresses the key MoO_3 modes. Previous reports have highlighted the reduction in Raman mode intensity with H_2-based reductions of MoO_3 to MoO_2.[25,29] Figure S5d (Supporting Information) quantifies the intensity suppression of the key MoO_3 Raman modes as a function of electron dose. We propose that this suppression is due to two reasons: reduction of the MoO_3 to MoO_{3-x} and local disorder introduced by the electron-beam. The emergence of MoO_2 Raman peaks was not observed; this suggests no phase change occurred in the dose regime examined in this paper. This is expected as the electron-beam doses required for phase transformation from MoO_3 to MoO_2 in previous electron microscopy studies were 10^5 times higher than the electron-beam doses applied in the present SEM experiments.[17,18] Detailed in situ scanning transmission electron microscopy (STEM)–EELS studies were undertaken in the low-dose regime to confirm and expand upon this result.

4.2. In Situ STEM–EELS Studies

In order to gain further insight on the effect of electron irradiation on the local chemistry, EELS spectra were recorded at regular time intervals during a low-dose irradiation process (432 $\mu C\,cm^{-2}\,S^{-1}$) in a STEM microscope. EELS is a technique of choice to get local (even atomic level) chemical information from nanostructures.[20,30,31] In particular, a wealth of precise and accurate chemical information on molybdenum oxides can be extracted from the conjugated analyses of the O-K and Mo-$M_{2,3}$ edges.[32]

Figure 4a shows the EELS core-loss spectra of a 2D nanosheet taken as a function of the irradiation time. The thickness of the corresponding nanosheet has been estimated from the low-loss monochromated EELS spectra and is between 8 and 10 nm. Figure S6 (Supporting Information) shows the carbon K-edge intensity does not increase with irradiation time, indicating no significant carbon contribution to EELS spectra changes.

A variety of EELS results show that low-dose electron irradiation of MoO_3 produces substoichiometric MoO_{3-x}. The O-K
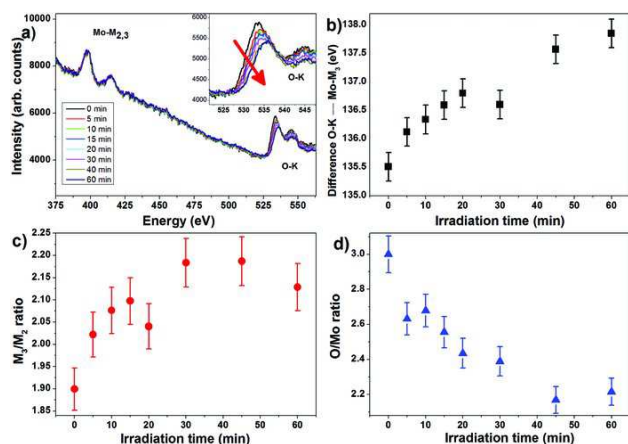
www.afm-journal.de

Full Paper

Figure 4. a) EELS core-loss spectra of a 2D nanosheet showing the Mo-M_3 and the O-K edge. The spectra were taken as a function of the irradiation time in the low-dose regime (dose $= 432 \ \mu C \ cm^{-2} \ S^{-1}$). The inset shows a magnified view of the spectra close to the O-K edge. The red arrow highlights the shift to higher energy and the intensity decrease of the O-K prepeak. b) Energy difference between the maxima of the O-K edge prepeak and the maximum of the Mo-M_3 edge as a function of the irradiation time. c) Mo-M_3/M_2 intensity ratio as a function of the irradiation time. d) O/Mo ratio as determined by EELS elemental quantification as a function of the irradiation time.

prepeak shift to higher energy (inset of Figure 4a) indicates a lower oxidation state of the transition metal linked to the oxygen atoms.[33] In accordance with reference,[32] an increase in the difference between the O-K edge and the Mo-M_3 edge and an increase in the Mo-M_3/M_2 ratio both indicate a lower Mo-oxidation state. Electron irradiation of the few-layer sample led to the expected reduction in Mo oxidation state, as shown by the increasing values with irradiation time in Figure 4b,c. The decrease of the O-K edge integrated intensity with irradiation (inset of Figure 4a) indicates oxygen loss. To quantify this process, the O/Mo ratio was derived by using a pristine sample as reference to extract the *k*-factors (Figure 4d). The O/Mo ratio decreases with the irradiation time and is equal to 2.6 and 2.2 after 5 and 60 min of irradiation, respectively. It is important to note that the fine structures of the O-K edge remain the same (except for the prepeak shift) during the whole experiment (inset of Figure 4a) and that they do not agree with the MoO_2 or the MoO phases[18] but correspond to the MoO_3 phase.[32] These results confirm the creation of oxygen vacancies induced by the electron-beam in the low-dose regime, rather than a phase transformation.

Figure 5a shows the low-loss EELS spectra taken with a monochromated electron-beam on an unirradiated and an irradiated area (after 60 min) of the same nanosheet. For comparison, a low-loss spectrum of bulk α-MoO_3 taken from reference[34] is also displayed. The energy-loss structures of the unirradiated area match well with those of bulk MoO_3, with a key difference in the A structure energy (5.8 eV for few-layer and 6.9 eV for bulk), although we should be cautious about
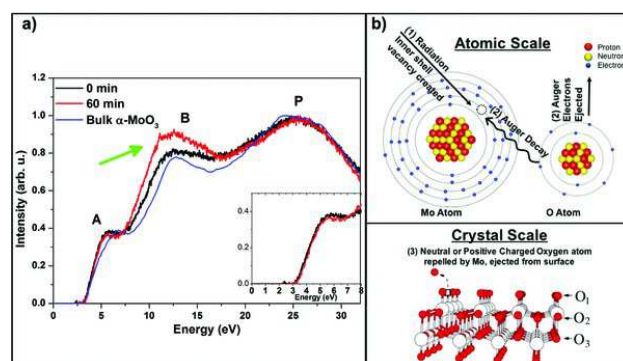

Figure 5. a) Low-loss EELS spectra taken from an unirradiated and an irradiated area (after 60 min) of the same nanosheet. The spectra were taken with the monochromator on (resolution $\approx$ 270 meV). For comparison, the low-loss EELS spectra taken from reference[34] are also given in blue (resolution 0.8 eV). The green arrow highlights the presence of another contribution in the B structure for the irradiated area. The inset shows a magnified view of the bandgap area. b) Schematic of Knotek–Feibelman mechanism at the atomic and crystal length scales.

comparison of spectra recorded with different microscopes. After 60 min of electron irradiation at low-dose, the low-loss spectrum is only slightly modified, further discounting the possibility of a phase transformation during low-dose irradiation. It should be noted that both, the unirradiated and irradiated low-loss spectra do not match the spectrum of MoO_2.[35] The A and P structures remain at the same energy but another contribution on the left side of the B structure can be highlighted (green arrow in Figure 5a). The B structure corresponds to a plasmon whose shape and intensity are strongly influenced by the presence of interband transitions linked to oxygen states.[34] The modification of the B structure could thus be due to the introduction of oxygen vacancies in the 2D MoO_3 nanosheet.

Finally, the bandgap was derived by performing a linear fit for the unirradiated and irradiated areas (inset of Figure 5a) and, for both cases, was found equal to 3.2 eV. This result is important because it is in excellent agreement with experimental values for bulk MoO_3[2] and thus confirms that the 2D nanostructuring of MoO_3 does not significantly alter the bandgap magnitude as highlighted by the present DFT calculations. It also confirms recent theoretical findings showing that the introduction of vacancies in MoO_3 does not alter the width of the bandgap but gives rise to gap states.[22] The analysis of the core-loss and low-loss spectra thus highlights that electron irradiation at low-dose of few-layer MoO_3 leads to the creation of oxygen vacancies in the MoO_3 network. These vacancies are therefore responsible for the increase of the conductance observed during the electrical measurements.

5. Mechanism of MoO_3 Reduction

The mechanism of the oxygen vacancy introduction is proposed to be the Knotek–Feibelman mechanism for radiolysis, as de-
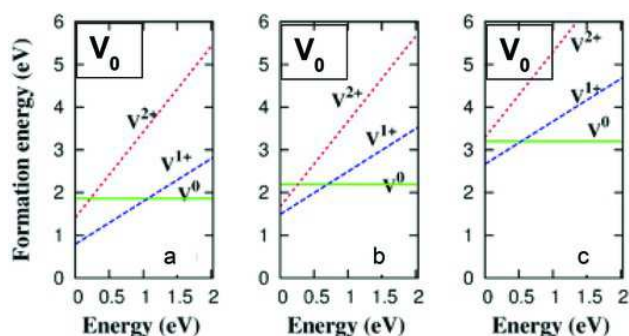
ADVANCED FUNCTIONAL MATERIALS

Author Proof

Full Paper

Figure 6. Oxygen vacancy formation energies as a function of Fermi level. a) V_{O1}, position O_1 vacancy, where the oxygen vacancy leads to the two donated electrons being localized on a single Mo center reducing it to Mo^{4+}. b) V_{O2}, The doubly coordinated O_2 vacancy leads to a polaron in which the two excess electrons localize on two surrounding Mo atoms. c) The triply coordinated O_3 vacancy also leads to a bipolaron, forming two Mo^{5+} sitting on opposite sides of the vacancy.

picted in Figure 5b. In this mechanism, the incident electron radiation creates an inner shell hole on the Mo site (Step 1 in the schematic). Next, an electron from a nearby oxygen atom has an interatomic Auger decay to the Mo inner shell hole, and further Auger electrons are ejected from the oxygen atom (Step 2). At the crystal level, neutral or positive oxygen atoms are then repelled by the surrounding molybdenum atoms and are ejected from the surface (Step 3) until the sheet becomes conductive enough to screen the oxygen ions.[36] The oxygen vacancy gives rise to n-type doping behavior due to the presence of two leftover electrons per oxygen vacancy. The outlined mechanism aligns nicely with the transport data. Oxygen vacancies are introduced, n-type doping the material to much higher currents until the MoO_3 nanosheet samples are sufficiently conducting to screen the oxygen atoms.

It is instructive to consider which crystallographic oxygen positions are favored for creating oxygen vacancies. DFT+U calculations were performed to calculate the energy of formation of oxygen vacancies at the different crystallographic positions (O_1, O_2, and O_3 from Figure 1) in a monolayer, as shown in **Figure 6**. The figure shows for each crystallographic vacancy position which resulting polaron or a local polarization coupled to an electron is most stable as a function of Fermi level. More details on each polaron condition (V^o, V^{1+}, V^{2+}) are given in the Supporting Information. Our DFT+U calculations indicate that the terminal O_1 oxygen has the smallest formation energy (E^f_{VO1}) for all accessible Fermi levels and charge states. For the neutral case, these energies are ordered such that $E^f_{VO1} < E^f_{VO2} < E^f_{VO3}$ with calculated values of 1.85, 2.19, and 3.20 eV, respectively. This trend is similar to previous calculations by Tahini et al. on the bulk case, where the corresponding formation energies are 2.06, 2.86, and 3.93 eV.[37] From these values we see that V_{O1} has a lower vacancy formation energy in 2D form (compared to bulk). During the reduction process, point defects should be favored by the terminal O_1 oxygens.

Combined, these results show that we can synthesize 2D MoO_3 and controllably introduce different levels of oxygen vacancies via the electron-beam, thereby tuning the electronic properties of few-layer MoO_3. This shows that few-layer MoO_{3-x} can be utilized as a functional electronic material in 2D form. Further, in situ EELS studies and accompanying mechanism give quantitative insight into the MoO_{3-x} reduction process and corresponding measurable signatures (transport, Raman modes, EELS spectra).

6. Conclusion

Recent reports have highlighted the ultrahigh mobility and promising transport characteristics of layered MoO_{3-x}, but full exploration of the few-layer properties has been hindered by the lack of a direct, vapor-phase growth. We report a facile PVD synthesis of high-quality, few-layer MoO_3 directly on SiO_2/Si substrates, enabling study of its exciting electronic properties. DFT+U calculations give insight into the electronic structure of the 2D MoO_3, showing that 2D confinement leads to a modest increase in bandgap. This modest increase is because the CBM and VBM are comprised of electronic states that are largely screened from confinement effects.

An electron-beam irradiation technique for introducing dose-controlled amounts of oxygen vacancies into the few-layer MoO_3, forming n-type doped MoO_{3-x}, is presented. Combining in situ transport and STEM–EELS studies, we present a detailed structure–property relationship between the Mo-oxidation state reduction and decreased resistance in few-layer MoO_{3-x}. Few-layer MoO_{3-x} transport properties are reported for sheets down to trilayer thickness, the most 2D-like reported hitherto. The n-type doping process is further correlated with Raman mode suppression. Supporting these experimental results, a radiolysis-based reduction mechanism is developed in detail. DFT+U calculations inform which crystallographic oxygen positions are most energetically favored during the oxygen vacancy introduction process in 2D MoO_3.

Few-layer MoO_3 shows enormous potential to be incorporated into 2D heterostructures and devices. For example, 2D MoO_3 could be used to hole-dope adjacent 2D materials, lowering contact resistance and creating 2D p–n junctions.[13, 27, 38] These results lay the groundwork and provide a simple synthesis to start investigations of integrating 2D MoO_3 into fully 2D heterostructures. This report provides an additional technique to create substoichiometric 2D MoO_{3-x} to serve as an active n-type 2D material and a thorough understanding of the modifications induced by low-dose electron irradiation on the local chemistry.

7. Experimental Section

Synthesis: MoO_3 sheets were grown in a 12″ Lindberg tube furnace. 50 mg of MoO_3 purchased from Sigma Aldrich (99.99%) was placed inside of an alumina boat in the hot zone of a furnace within a 1″ silica tube. 300 nm $SiO2$/degenerately doped Si substrates were placed downstream in a colder zone within

the furnace ($\approx$4 cm from center), suspended on top of alumina boats. The chamber pressure was kept at 2.8 Torr with a flow rate of 18 sccm of ultradry air serving as the carrier gas. The furnace was heated to 675 °C over 25 min, then to 700 °C over 5 min, before quenching by opening the furnace.

(S)TEM and EELS: Preliminary TEM studies were carried out using a JEOL 2100 microscope at 200 kV. The influence of electron irradiation at low dose on the local chemistry of 2D MoO_3 was studied by using an FEI Titan Low-Base microscope operated at 80 kV and equipped with a Cs probe corrector, a monochromator, an ultrabright X-FEG electron source, and a Gatan Tridiem ESR 865 EELS spectrometer. The electron dose during electron irradiation was equal to 432 μC cm^{-2} S^{-1} and the irradiation time was up to 60 min. During irradiation, core-loss EELS spectra were collected in STEM mode, the energy resolution was 1 eV with a dispersion of 0.73 eV per pixel and the acquisition time was about 0.5 s per pixel (total acquisition time $\approx$40 s). With this setup, the convergence and collection angles were 36 and 51 mrad, respectively. To increase the signal/noise ratio the EELS spectra were recorded in spectrum image mode[31,39] and the datasets were then denoised with the open-source program Hyperspy by using principal component analysis routines.[31,40] To minimize the systematic error from peak positions, the maximum of the $Mo-M_3$ edges was first aligned to the same energy loss (397.8 eV). Then, determination of the $Mo-M_3/M_2$ ratio and O/Mo elemental quantification were performed following the methodology described in Lajaunie et al.[32] In particular, the determination of the *k*-factors was done by using the unirradiated sample as reference and by using an energy window of 15 eV as it yields the best precision for elemental quantification. Low-loss spectra were also acquired on the same nanosheets with the monochromator on. In this case, the energy resolution was about 270 meV with a dispersion of 0.02 eV per pixel. The relative thickness t/λ was calculated by using the Fourier-log algorithm.[41] For this purpose, a zero-loss peak (ZLP) taken in the vacuum in the same experimental conditions. The absolute thickness was then determined by estimating λ with the modified Iakoubovskii formula that yielded a value of λ = 98 nm for α-MoO_3.[41,42] This method has been shown to yield a reasonable estimation of absolute thickness.[34] After subtraction of the ZLP, the bandgap was determined by using the linear fitting method, which yields reliable results for monochromated spectra.[43] The most representative spectra were submitted to the EELS Database as references.[35]

Raman Spectroscopy: Raman spectra were taken on Horiba LabRAM HR Evolution. Spectra were taken with a 532 nm excitation laser with a max power of 50 mW, with neutral density filters at 0.1% (5 min × 2). Backgrounds were fitted and subtracted to highlight the key features.

In Situ Transport: In situ electron-beam irradiation and transport measurements were taken using a Kleindiek nanomanipulation system in an FEI Helios Nanolab SEM/FIB. Electrical measurements were taken with a Keithley 4200 Semiconductor Characterization System. Tungsten probes (Micromanipulator, model 7×) were coated with 100 nm Au to improve contact resistance.

Theoretical Calculations (DFT + U, oxygen vacancy formation energies, Boltzmann transport): Details on all theoretical calculations can be found in the Supporting Information.

Supporting Information

Supporting Information is available from the Wiley Online Library or from the author.

Acknowledgements

[1] S. Cong, T. Sugahara, T. Wei, J. Jiu, Y. Hirose, S. Nagao, K. Suganuma, *Cryst. Growth Des.* **2015**, *15*, 4536.

[2] D. O. Scanlon, G. W. Watson, D. Payne, G. Atkinson, R. Egdell, D. Law, *J. Phys. Chem. C* **2010**, *114*, 4636.

[3] R. Naouel, H. Dhaouadi, F. Touati, N. Gharbi, *Nano-Micro Lett.* **2011**, *3*, 242.

[4] M. Vasilopoulou, A. M. Douvas, D. G. Georgiadou, L. C. Palilis, S. Kennou, L. Sygellou, A. Soultati, I. Kostis, G. Papadimitropoulos, D. Davazoglou, *J. Am. Chem. Soc.* **2012**, *134*, 16178.

[5] K. W. Harrison, C. D. Corolewski, M. D. McCluskey, J. Lindemuth, S. Ha, M. G. Norton, *J. Mater. Sci.: Mater. Electron.* **2015**, *26*, 9717.

Q4

ADVANCED FUNCTIONAL MATERIALS

Author Proof

www.afm-journal.de

Full Paper

[6] a) S. Cong, T. Sugahara, T. Wei, J. Jiu, Y. Hirose, S. Nagao, K. Suganuma, *Adv. Mater. Interfaces* **2016**, *3*; b) L. Zhou, L. Yang, P. Yuan, J. Zou, Y. Wu, C. Yu, *J. Phys. Chem. C* **2010**, *114*, 21868; c) A. Guerfi, R. Paynter, L. H. Dao, *J. Electrochem. Soc.* **1995**, *142*, 3457.

[7] a) C. Battaglia, X. Yin, M. Zheng, I. D. Sharp, T. Chen, S. McDonnell, A. Azcatl, C. Carraro, B. Ma, R. Maboudian, *Nano Lett.* **2014**, *14*, 967; b) M. T. Greiner, L. Chai, M. G. Helander, W. M. Tang, Z. H. Lu, *Adv. Funct. Mater.* **2013**, *23*, 215; c) S. Höfle, H. Do, E. Mankel, M. Pfaff, Z. Zhang, D. Bahro, T. Mayer, W. Jaegermann, D. Gerthsen, C. Feldmann, *Org. Electron.* **2013**, *14*, 1820.

[8] S. Balendhran, J. Deng, J. Z. Ou, S. Walia, J. Scott, J. Tang, K. L. Wang, M. R. Field, S. Russo, S. Zhuiykov, *Adv. Mater.* **2013**, *25*, 109.

[9] D. Xiang, C. Han, J. Zhang, W. Chen, *Sci. Rep.* **2014**, *4*, 4891.

[10] M. M. Alsaif, K. Latham, M. R. Field, D. D. Yao, N. V. Medehkar, G. A. Beane, R. B. Kaner, S. P. Russo, J. Z. Ou, K. Kalantar-zadeh, *Adv. Mater.* **2014**, *26*, 3931.

[11] M. M. Y. A. Alsaif, A. F. Chrimes, T. Daeneke, S. Balendhran, D. O. Bellisario, Y. Son, M. R. Field, W. Zhang, H. Nili, E. P. Nguyen, K. Latham, J. van Embden, M. S. Strano, J. Z. Ou, K. Kalantar-zadeh, *Adv. Funct. Mater.* **2016**, *26*, 91.

[12] a) S. McDonnell, A. Azcatl, R. Addou, C. Gong, C. Battaglia, S. Chuang, K. Cho, A. Javey, R. M. Wallace, *ACS Nano* **2014**, *8*, 6265; b) Z. Chen, I. Santoso, R. Wang, L. F. Xie, H. Y. Mao, H. Huang, Y. Z. Wang, X. Y. Gao, Z. K. Chen, D. Ma, *Appl. Phys. Lett.* **2010**, *96*, 213104.

[13] S. Chuang, C. Battaglia, A. Azcatl, S. McDonnell, J. S. Kang, X. Yin, M. Tosun, R. Kapadia, H. Fang, R. M. Wallace, A. Javey, *Nano Lett.* **2014**, *14*, 1337.

[14] K. Kalantar-Zadeh, J. Tang, M. Wang, K. L. Wang, A. Shailos, K. Galatsis, R. Kojima, V. Strong, A. Lech, W. Wlodarski, *Nanoscale* **2010**, *2*, 429.

[15] H. Bai, W. Yi, J. Li, G. Xi, Y. Li, H. Yang, J. Liu, *J. Mater. Chem. A* **2016**, *4*, 1566.

[16] D. J. Late, B. Liu, H. Matte, C. Rao, V. P. Dravid, *Adv. Funct. Mater.* **2012**, *22*, 1894.

[17] D. E. Diaz-Droguett, A. Zuniga, G. Solorzano, V. Fuenzalida, *J. Nanopart. Res.* **2012**, *14*, 1.

[18] D. Wang, D. S. Su, R. Schlögl, *Zeitschrift für Anorganische und Allgemeine Chemie* **2004**, *630*, 1007.

[19] a) F. Banhart, *In-situ Electron Microscopy at High Resolution*, World Scientific, **2008**; b) A. Krasheninnikov, K. Nordlund, *J. Appl. Phys.* **2010**, *107*, 071301.

[20] R. Arenal, X. Blase, A. Loiseau, *Adv. Phys.* **2010**, *59*, 101.

[21] J. W. Rabalais, R. J. Colton, A. M. Guzman, *Chem. Phys. Lett.* **1974**, *29*, 131.

[22] K. Inzani, T. Grande, F. Vullum-Bruer, S. M. Selbach, *J. Phys. Chem. C* **2016**, *120*, 8959.

[23] R. Coquet, D. J. Willock, *Phys. Chem. Chem. Phys.* **2005**, *7*, 3819.

[24] M. Cahay, presented at Proc. Int. Symp. on Quantum Confinement VI: Nanostructured Materials and Devices, **2001**.

[25] W. Xie, M. Su, Z. Zheng, Y. Wang, L. Gong, F. Xie, W. Zhang, Z. Luo, J. Y. Luo, P. Liu, *ACS Nano* **2016**, *10*, 1662.

[26] M. Camacho-López, L. Escobar-Alarcón, M. Picquart, R. Arroyo, G. Córdoba, E. Haro-Poniatowski, *Opt. Mater.* **2011**, *33*, 480.

[27] A. J. Molina-Mendoza, J. L. Lado, J. O. Island, M. A. Niño, L. Aballe, M. Foerster, F. Y. Bruno, A. López-Moreno, L. Vaquero-Garzon, H. S. J. van der Zant, G. Rubio-Bollinger, N. Agraït, E. M. Pérez, J. Fernández-Rossier, A. Castellanos-Gomez, *Chem. Mater.* **2016**, *28*, 4042.

[28] C. Julien, G. Nazri, *Solid State Ionics* **1994**, *68*, 111.

[29] J. Z. Ou, J. L. Campbell, D. Yao, W. Wlodarski, K. Kalantar-Zadeh, *J. Phys. Chem. C* **2011**, *115*, 10757.

[30] a) L. S. Panchakarla, L. Lajaunie, R. Tenne, R. Arenal, *J. Phys. Chem. C* **2016**, *120*, 15600; b) L. S. Panchakarla, L. Lajaunie, A. Ramasubramaniam, R. Arenal, R. Tenne, *ACS Nano* **2016**, *10*, 6248; c) F. L. Deepak, A. Mayoral, R. Arenal, *Advanced Transmission Electron Microscopy*, Springer, **2015**; d) R. Arenal, K. March, C. P. Ewels, X. Rocquefelte, M. Kociak, A. Loiseau, O. Stéphan, *Nano Lett.* **2014**, *14*, 5509.

[31] R. Arenal, F. De la Pena, O. Stephan, M. Walls, M. Tence, A. Loiseau, C. Colliex, *Ultramicroscopy* **2008**, *109*, 32.

[32] L. Lajaunie, F. Boucher, R. Dessapt, P. Moreau, *Ultramicroscopy* **2015**, *149*, 1.

[33] a) G. Botton, C. Appel, A. Horsewell, W. Stobbs, *J. Microscopy* **1995**, *180*, 211; b) Z. Wang, N. Dupré, L. Lajaunie, P. Moreau, J.-F. Martin, L. Boutafa, S. Patoux, D. Guyomard, *J. Power Sources* **2012**, *215*, 170.

[34] L. Lajaunie, F. Boucher, R. Dessapt, P. Moreau, *Phys. Rev. B* **2013**, *88*, 115141.

[35] P. Ewels, T. Sikora, V. Serin, C. P. Ewels, L. Lajaunie, *Microsc. Microanal.* **2016**, *22*, 717.

[36] R. Egerton, P. Li, M. Malac, *Micron* **2004**, *35*, 399.

[37] H. A. Tahini, X. Tan, S. N. Lou, J. Scott, R. Amal, Y. H. Ng, S. C. Smith, *ACS Appl. Mater. Interfaces* **2016**, *8*, 10911.

[38] J. D. Cain, E. D. Hanson, F. Shi, V. P. Dravid, *Curr. Opin. Solid State Mater. Sci.*

[39] C. Jeanguillaume, C. Colliex, *Ultramicroscopy* **1989**, *28*, 252.

[40] F. De la Peña, P. Burdet, T. Ostasevicius, M. Sarahan, M. Nprd, V. T. F. J. Taillon, A. Eljarrat, S. Mazzucco, G. Donvail, L. F. Zagonel, M. Walls, I. Iyengar, **2015**.

[41] R. F. Egerton, *Electron Energy-Loss Spectroscopy in the Electron Microscope*, Springer Science & Business Media, **2011**.

[42] K. Iakoubovskii, K. Mitsuishi, Y. Nakayama, K. Furuya, *Microsc. Res. Tech.* **2008**, *71*, 626.

[43] a) J. Park, S. Heo, J.-G. Chung, H. Kim, H. Lee, K. Kim, G.-S. Park, *Ultramicroscopy* **2009**, *109*, 1183; b) R. Arenal, O. Stéphan, M. Kociak, D. Taverna, A. Loiseau, C. Colliex, *Phys. Rev. Lett.* **2005**, *95*, 127601.

Q5 Q6 Q7 Q8 Q9

Q1   APT to AU: Please provide the highest academic title (either Dr. or Prof.) for all authors, where applicable.

Q2   APT to AU: If you have not returned the color cost confirmation form already, please email the completed form to the editorial office when you submit your proof corrections. This will confirm that you are willing to support the cost for color publication of the figures. Details about our color policies and a link to the form were included with your acceptance email. If you wish for your figures to be presented in grayscale, please email the editorial office to confirm this.

Q3   APT to AU: Figure quality is not good in figure 6. Please check

Q4   APT to AU: Please define 'FIB' at its first occurrence in the text.

Q5   APT to AU: Please provide the page number in ref. (6a).

Q6   APT to AU: Please provide the publisher location in refs. (19a,30c,41).

Q7   APT to AU: Ref. (33) is not cited in the text. Please cite it in sequence in the text.

Q8   APT to AU: Please provide year, volume number, and page number in ref. (40).

Q9   APT to AU: Please provide the complete bibliographic details in ref. (40).